Diffusion MRI marks progressive alterations in fiber integrity in the zQ175DN mouse model of Huntington's disease

Nicholas Vidas-Guscic [a,b,1,*], Joëlle van Rijswijk [a,b,1], Johan Van Audekerke [a,b], Ben Jeurissen [b,c,d], Israel Nnah [e], Haiying Tang [f], Ignacio Muñoz-Sanjuan [f], Dorian Pustina [f], Roger Cachope [f], Annemie Van der Linden [a,b], Daniele Bertoglio [a,b], Marleen Verhoye [a,b]

[a] Bio-Imaging Lab, University of Antwerp, Antwerp, Belgium
[b] µNeuro Center for Excellence, University of Antwerp, Antwerp, Belgium
[c] Vision Lab, University of Antwerp, Antwerp, Belgium
[d] Lab for Equilibrium Investigations and Aerospace, University of Antwerp, Antwerp, Belgium
[e] Charles River Laboratories, Shrewsbury, MA, United states
[f] CHDI Management, Inc., the company that manages the scientific activities of CHDI Foundation, Inc., Princeton, NJ, United States

ARTICLE INFO

ABSTRACT

Huntington's disease (HD) is a progressive neurodegenerative disease affecting motor and cognitive abilities. Multiple studies have found white matter anomalies in HD-affected humans and animal models of HD. The identification of sensitive white-matter-based biomarkers in HD animal models will be important in understanding disease mechanisms and testing the efficacy of therapeutic interventions. Here we investigated the progression of white matter deficits in the knock-in zQ175DN heterozygous (HET) mouse model of HD at 3, 6 and 11 months of age (M), reflecting different states of phenotypic progression. We compared findings from traditional diffusion tensor imaging (DTI) and advanced fixel-based analysis (FBA) diffusion metrics for their sensitivity in detecting white matter anomalies in the striatum, motor cortex, and segments of the corpus callosum. FBA metrics revealed progressive and widespread reductions of fiber cross-section and fiber density in myelinated bundles of HET mice. The corpus callosum genu was the most affected structure in HET mice at 6 and 11 M based on the DTI and FBA metrics, while the striatum showed the earliest progressive differences starting at 3 M based on the FBA metrics. Overall, FBA metrics detected earlier and more prominent alterations in myelinated fiber bundles compared to the DTI metrics. Luxol fast blue staining showed no loss in myelin density, indicating that diffusion anomalies could not be explained by myelin reduction but diffusion anomalies in HET mice were accompanied by increased levels of neurofilament light chain protein at 11 M. Altogether, our findings reveal progressive alterations in myelinated fiber bundles that can be measured using diffusion MRI, representing a candidate noninvasive imaging biomarker to study phenotype progression and the efficacy of therapeutic interventions in zQ175DN mice. Moreover, our study exposed higher sensitivity of FBA than DTI metrics, suggesting a potential benefit of adopting these advanced metrics in other contexts, including biomarker development in humans.

1. Introduction

Huntington's disease (HD) is a progressive genetic neurological disease that affects the motor and cognitive abilities of people with HD (PwHD) (Bates et al., 2015; Snowden, 2017). HD is caused by an expansion in the CAG trinucleotide repeat of the huntingtin gene (*HTT*), leading to the expression of toxic mutant huntingtin (mHTT) (MacDonald et al., 1993). The medium-sized spiny neurons of the striatum are most vulnerable to the toxic properties of mHTT, causing atrophy of the striatum and leading to motor dysfunction, a hallmark clinical sign of the disease (Fazl and Fleisher, 2018; Vonsattel et al., 1985; Wild et al., 2010).

Currently, there are no disease-modifying treatments available (Estevez-Fraga et al., 2020; Ferguson et al., 2022). To assess the efficacy

---

of the current therapeutic strategies, animal models play a crucial role, and biomarkers are needed to identify specific anomalies or their mitigation post-intervention. The successful utilization of animal models depends on (1) model phenotypes that resemble the human phenotype that are (2) governed by analogous underlying pathologic mechanisms, and (3) the availability of markers that can measure the progression and modification of disease.

The zQ175DN heterozygous (HET) mouse model is a genetically precise knock-in mouse model of the CAG expansion responsible for HD, in which exon 1 of human *HTT* (containing ~190 trinucleotide CAG repeats) was knocked into the endogenous murine *Htt* gene. zQ175DN mice are a subtle modification of the original zQ175 mouse model (Heikkinen et al., 2012; Menalled et al., 2012), in which the retained 5′ neomycin cassette from the original line was removed (Farshim and Bates, 2018). They show progressive striatal projection neuron (medium spiny neuron) abnormalities and striatal volume loss (Deng et al., 2021; Goodliffe et al., 2019), complex alterations in basal ganglia indirect pathway activity (Atherton et al., 2016; Callahan et al., 2022), widespread HTT aggregate pathology (Herrmann et al., 2021; Smith et al., 2014), and extensive striatal transcriptional and proteomic dysregulation that is similar to the one that PwHD exhibit (Langfelder et al., 2016; Lee et al., 2020). Behaviorally, zQ175 / zQ175DN mice exhibit progressive circadian dysfunction (Smarr et al., 2019) and other subtle behavioral manifestations indicative of cortico-basal ganglia circuit impairments, including amotivation/apathy (Covey et al., 2016; Oakeshott et al., 2012), cognitive impairment (Piiponniemi et al., 2018), gait abnormalities and hypo-locomotor phenotypes (Beaumont et al., 2016; Heikkinen et al., 2020a; Smith et al., 2014). Unlike PwHD - but in common with other HD mouse models - striatal atrophy appears largely due to cell shrinkage and neuropil loss, rather than overt cellular neurodegeneration, suggestive that HD mouse models likely model an early stage of HD pathology throughout their lifespan (Deng et al., 2021).

Since zQ175DN is already well studied for its phenotypic and neuropathologic similarity with the human disease, our study focuses on the third point, that is, the identification of biomarkers.

In PwHD, white matter shows prominent anomalies, and there is evidence that some of these anomalies may precede the typical striatal volume loss (Byrne et al., 2018; Casella et al., 2020). The measurement of neurofilament light chain (NfL) protein, a known indicator of axonal damage, indicates that axonal damage occurs very early, before volumetric atrophy emerges (Byrne et al., 2018). Moreover, NfL levels are a good predictor of future atrophy (Johnson et al., 2018).

We therefore aimed to investigate longitudinally the zQ175DN mouse model utilizing state-of-the-art MRI techniques and analytical tools to determine whether we could detect microstructural anomalies in myelinated fiber bundles. Diffusion tensor imaging (DTI) has been widely applied in HD studies before (Casella et al., 2020; Estevez-Fraga et al., 2021), but the conventional diffusion tensor model is limited in its ability to disentangle meaningful information from derived metrics in the presence of crossing-fibers (Jeurissen, Tournier, et al., 2014). Techniques such as constrained spherical deconvolution (CSD) have been developed to address the issue of crossing-fibers by separating the diffusion-weighted signal into fiber bundles (Jeurissen et al., 2014b; Tournier et al., 2004, 2007), and CSD has been demonstrated to improve the correlation between pathology and microstructure in crossing tracts (Reijmer et al., 2012). The fixel-based analysis (FBA) method uses CSD to extract different fiber orientations and generate multiple fiber elements (fixels) that contain detailed information on the macrostructure (fiber cross-section (FC)) and microstructure (fiber density (FD), intra-axonal volume) of fiber tracts, and a combined fiber density and cross-section (FDC) metric (Raffelt et al., 2017b). Recently, FBA has been used to identify fiber bundles (systems) that are altered in PwHD before (Zeun et al., 2022) and after (Adanyeguh et al., 2021; Oh et al., 2021) clinical motor diagnosis. These studies reveal that in PwHD, FBA metrics are reduced in the cortico-spinal tract (Adanyeguh et al., 2021; Oh et al., 2021; Zeun et al., 2022), and are correlated to clinical outcome

measures (Adanyeguh et al., 2021; Zeun et al., 2022). Also, in other neurodegenerative disorders such as Parkinson's disease, Alzheimers disease, Spinocerebellar Ataxia, and Multiple Sclerosis, decreases in FBA metrics are often reported (see review Dhollander et al., 2021a). However, while FBA has been used in clinical studies, to date there are no studies that have used FBA to investigate animal models of HD.

Our study had three objectives: to (1) investigate the brain fiber microstructural anomalies in zQ175DN compared to wildtype (WT) littermates, (2) characterize the temporal changes to identify potential biomarkers of disease progression, and (3) determine whether FBA has greater sensitivity compared to the DTI approach. Additionally, we have performed analysis of plasma NfL and myelin density using Luxol Fast Blue (LFB). We predicted that zQ175DN mice may develop structural anomalies with age and that regional changes would precede global microstructural alterations at later ages. We also predict that improved modeling of the diffusion MRI (dMRI) data may detect those anomalies with more sensitivity than the traditional DTI.

2. Methods

2.1. Animals

Thirthy WT and 30 HET male zQ175DN knock-in mice on a congenic C57Bl/6J background (B6.129S1-*Htt*^tm1.1Mfc^/190ChdiJ JAX stock #029928) were longitudinally scanned, of which 3 WT and 2 HET mice were excluded from the analysis due to a brain aneurysm (WT, *n* = 1), image artifacts (WT, *n* = 2), and genotype inconsistency (HET, n = 2). Hence, 20 mice were scanned at 3, 6 and 11 months of age. Seven WT and 8 HET animals were only scanned at 3 and 6 months, as 9 WT and 9 HET mice were already scanned at 11 months of age (**Supplementary Fig. 1**). Mice were obtained from Jackson Laboratories (Maine, USA). Due to sporadic congenital portosystemic shunt occurring in C57Bl/6J mice (Cudalbu et al., 2013), all animals were screened at Jackson Laboratories before shipment to avoid this confounding factor; hence, all animals used in this study were shunt-free. Mice were genotyped at birth and after experiments to determine their number of CAG repeats (WT = 7/7 CAG repeats, HET = 7/194 ± 3 CAG repeats).

All animals were single-housed at the central housing facility of the University of Antwerp on a 12-h light-dark cycle in climate-controlled rooms. Food and water were provided ad libitum. All experimental procedures and animal handling described in this investigation were carried out according to European guidelines for the housing and use of laboratory animals (2010/63/EEC). This project was approved by the ethical committee on animal care and use at the University of Antwerp, Belgium (ECD 2017–09 and 2020–33).

2.2. MRI acquisition

Animals were anesthetized using 4% isoflurane (IsoFlo, Abbott Laboratories Ltd., USA) for induction and 1–2% for maintenance in a gaseous mixture of 70% N_2 and 30% O_2 delivered to the animal at a flow rate of 600 mL/min. After induction, the mice were placed in a dedicated stereotactic setup that restricts movement. The animal's breathing rate and body temperature were continuously monitored throughout the scanning procedure (SA Instruments, INC., USA). The breathing rate was maintained between 90 and 120 breaths per minute by adjusting the concentration of isoflurane and the body temperature was maintained at $(37.0 \pm 0.1)\,°C$ using a heated feedback control system (SA instruments, INC., USA).

Diffusion-weighted images were acquired on a 7 T Pharmascan 70/16 horizontal MR system (Bruker, Germany) interfaced with Paravision 6 software (Bruker, Germany). A volume coil was used for radio frequency transmission and the signal was received using a four-channel array head receive coil. Diffusion-weighted two-shot spin-echo echo-planar imaging (SE-EPI) data were acquired (TE/TR = 23/7000 ms): consisting of 16 horizontal slices with an in-plane resolution of (200 ×

200)μm^2 and a slice thickness of 500 μm, matrix size = [108 × 100]. Diffusion weighting was achieved with a diffusion gradient duration (δ) of 4 ms and a separation (Δ) of 12 ms, *b*-values = 700, 1200, and 2800 s/mm^2 with 60 unique diffusion directions per shell and three additional *b*-value = 0 s/mm^2 images per shell. Six additional *b*-value = 0 s/mm^2 images were acquired with opposing phase encoding direction for distortion correction using topup (FSL). The total scantime for diffusion-weighted imaging was 49 min.

2.3. MRI processing

The gradient table of all diffusion datasets was checked and corrected in MRtrix3 (Jeurissen et al., 2014a). The complete dMRI image series was denoised in MRtrix3 (Veraart et al., 2016a, 2016b) and then corrected for Gibbs ringing artifacts in MRtrix3 (Kellner et al., 2016). The next step was a combined distortion, motion, and eddy current correction which includes an automated outlier slice detection algorithm using FSL6.0 software tools (Andersson et al., 2003; Andersson and Sotiropoulos, 2016; Skare and Bammer, 2009; Smith et al., 2004).

For FBA, pre-processed diffusion datasets were bias field corrected (N4 algorithm, ANTs) (Tustison et al., 2010). Then, group-averaged tissue response functions were estimated from dMRI data for the main tissue types; gray matter, white matter, and cerebrospinal fluid using an algorithm in MRtrix3 (D'hollander et al., 2016; Dhollander et al., 2019; Dhollander et al., 2021a; Jeurissen et al., 2014b). Diffusion-weighted images were up-sampled (MRtrix3) to an isotropic voxel size of 200 μm^3. Then, the fiber orientation distributions (FOD) were estimated using a multi-shell multi-tissue constrained spherical deconvolution algorithm (MSMT-CSD) (Jeurissen et al., 2014b; Tournier et al., 2004), resulting in tissue density maps for each compartment (white matter, gray matter, and cerebrospinal fluid), which were intensity normalized between tissue types (Dhollander et al., 2021b; Raffelt et al., 2017a).

The white matter, gray matter, and cerebrospinal fluid tissue density maps of five HET and five WT subjects were randomly selected per age to create unbiased multi-tissue (white matter, gray matter, and cerebrospinal fluid) templates using a combined non-linear (SyN) registration in ANTs. All white matter fiber orientation distributions (WMFOD) maps were warped to the WMFOD template and converted to an MRtrix3 compatible format.

The WMFOD template was thresholded to include FOD lobes with an amplitude higher than 0.1 to include only white matter containing voxels. In the next step, the fixels were indexed in these white matter voxels and the apparent fiber density images were assigned to each fixel (Raffelt et al., 2012). Individual WMFOD images were warped to the WMFOD study space without reorientation of the fixels. Then individual fixel maps were reoriented using the warps that were estimated during the spatial transformation step from individual WMFOD to template WMFOD space. The correspondence between the subject and the template fixels was determined and the FD value of a subject fixel was assigned to its corresponding fixel in the template space. The FC was estimated from the warp field that maps from the template to the subject space (i.e., a reverse mapping). Finally, the combined metric fiber density and fiber cross-section parametric fixel maps were created per subject by multiplying the FD and FC fixel maps.

A probabilistic 20 million streamline tractogram was generated in template space based on the WMFOD template using the iFOD2 algorithm (min/max tract length = 1/25 mm, maximal angular deviation per step size is 45°, and streamline termination for an FOD amplitude of 0.1) and filtered with the SIFT algorithm to two million streamlines in MRtrix3 (Smith et al., 2013). This tractogram was used to perform smoothing and connectivity-based fixel enhancement (CFE) (Raffelt et al., 2015) of fixel data (FD, FC, and FDC). This tractogram was further reduced to 200.000 randomly selected tracts for visualization.

For diffusion tensor analysis, the dataset was smoothed separately within each tissue type, i.e., the white and gray matter, to reduce information spillover, using a 400 μm full-width half maximum Gaussian

kernel in AFNI. Diffusion data were fitted to the diffusion kurtosis model in the subject space using Mrtrix3 (Basser et al., 1994; Veraart et al., 2013). Diffusion tensor metrics were calculated; fractional anisotropy (FA), mean diffusivity (MD), radial diffusivity (RD), and axial diffusivity (AD), and these parametric maps were warped to the template space for further analysis. Region-of-interest (ROI) and tract-of-interest (TOI) analysis were performed in whole brain white matter, corpus callosum (genu, body, and splenium), caudate putamen, and motor cortex, which have been often included as ROIs in human HD studies (Estevez-Fraga et al., 2021).

2.4. Plasma neurofilament light

NfL in plasma was assessed to determine its levels in relation to the observed alterations in fiber integrity. Blood samples were collected from all mice at 6 and 11 months of age via acute puncture of the submandibular vein. Mice were restrained to taut the skin over the mandible. An acute puncture of the submandibular vein was performed using a 5.5 mm lancet (Goldenrod, MEDIpoint). Blood was then collected in pre-chilled 250 μL K-EDTA coated microtubes (BD microtainer MAP, NJ, USA). Approximately 200 μL of whole blood was collected, to ensure that 50 μL of plasma could be collected and kept on ice. Blood samples were centrifuged within 15 min of collection at 4 °C with 5000 rpm for 5 min. Plasma was transferred to new labeled Eppendorf tubes chilled on dry ice and stored at -80 °C. Samples were shipped on dry ice and NfL concentration was analyzed at Charles Rivers Laboratories.

Plasma NfL levels were assessed using a factory validated- and Charles River Laboratories-qualified Simoa® NF-Light™ Advantage Kit (product #103186, Quanterix, MA, USA). Plasma samples were first diluted with the kit's NF-Light™ Sample Diluent (kit part #102252) at a 1/20 dilution factor and then analyzed with a fully automated Quanterix™ HD-X Analyzer™ (Quanterix, MA, USA). To process and analyze samples, the HD-X Analyzer™ instrument used a multi-array of femtoliter-sized reaction chambers that isolated and detected single NfL molecules bound to proprietary paramagnetic beads supplied with the assay kit (part #102246). Anti-NfL antibody-coated beads were incubated with NfL protein standards (Kit part #102255), quality controls (including high, mid and low quality controls and an endogenous matrix quality control), or diluted plasma samples. Each well containing beads was then incubated with a biotinylated anti-NfL detection antibody supplied with the kit (part #102248). Unbound antibody was removed by a series of washes with system wash buffers (product #101619 and #100205.2, respectively, Quanterix, MA, USA) and antibody-bound beads were then loaded into arrays of femtoliter-sized wells that held no more than one bead per well. β-galactosidase–labeled streptavidin (kit part #102250) was added, followed by addition of resorufin β-D-galactopyranoside substrate (kit part #103159). Wells were subsequently sealed with system sealing oil (product #100206, Quanterix, MA, USA) and the fluorescence signal digitally imaged by the Quanterix™ HD-X Analyzer™. A calibration curve was obtained by plotting the average number of enzymes per bead (AEB) signal against reference NfL protein concentrations. A five-parameter logistic (5PL) model was then used to fit the sigmoid calibration curve with a weighting factor of 1/Y2. The concentration (pg/mL) of NfL protein in plasma samples was determined by interpolation from the calibration curve.

2.5. Luxol Fast Blue staining

To assess whether the deficits observed in the corpus callosum genu were related to the total change in myelin concentration, we performed an LFB staining using the LBC-1 LFB staining kit (IMTEC Diagnostics N. V., Antwerp, Belgium) on fresh-frozen tissue from male zQ175DN HET mice at 6 (WT, *n* = 9; HET, n = 9) and 13 months (WT, *n* = 10; HET, *n* = 15) of age available from a previous study (Bertoglio et al., 2022a). Twenty μm-thick slices were air-dried for 5 min. The slices were then

rehydrated in Xylene and an ethanol gradient (100%, 96%, and 70%), and dH$_2$0. Slices were incubated in LFB at a constant temperature of 50 °C. Next, the tissue was washed in dH$_2$0. Tissue was differentiated in lithium carbonate (20 s) and in 70% ethanol (3 min). The tissue was washed twice in dH$_2$0 and then submersed in Cresyl Echt solution for 2 min. The tissue was then washed in 100% ethanol and dehydrated and coverslipped with DPX mountant. Microscopic images of all LFB stained slices were obtained using a BX51 fluorescence microscope equipped with an OlympusDP71 digital camera using 20 × (NA0.50) dry objective lens. Images were analyzed using ImageJ software (Schneider et al., 2012). First, images were converted from RGB to 8-bit and a mask was created for the corpus callosum genu. Particle analysis was performed to create a mask of the Cresyl violet stained cells, which was then removed from the corpus callosum genu mask to create a new mask only including the LFB-stained corpus callosum genu. The average image intensity was extracted from the corpus callosum genu in triplicate for each subject. The mean of each subject was used for quantification.

2.6. Statistical analysis

For whole brain fixel-based comparisons between HET vs WT, nonparametric two-tailed *t*-tests were performed per age using permutation (5000 permutations) testing (MRtrix3). Statistical parametric maps were thresholded for a *p*-value of $p < 0.05$ after connectivity-based fixel enhancement (CFE) with family-wise error (FWE) correction. Absolute effect sizes were mapped to the 200.000 streamline tractogram using MRtrix3 for visualization.

Tract editing was used to isolate the TOI and subsequently converted to fixels for mean value extraction. These were analyzed in GraphPad Prism 9 using a mixed-effects model with factors: genotype (two levels; WT and HET), age (three levels; 3, 6, and 11 months of age), and a random subject factor. Post-hoc testing was performed if a significant interaction was observed, which were corrected using FDR correction. If no significant interaction was observed, the interaction effect was removed from the model. FDR corrections were performed per main effect and interaction over the different brain regions. Group means and standard deviation are summarized in **Supplementary Tables 1 and 3**.

Statistical analysis of plasma NfL protein levels was performed in GraphPad Prism 9. Outlier detection was performed for each combination of genotype x age using the ROUT method in GraphPad Prism 9. Outliers were excluded from analysis, and the remaining data were analyzed using a mixed-effects model for the effects of age (6 and 11 months of age) and genotype (WT and HET), and a random subject factor, followed by post-hoc testing in the case of a significant interaction. If no significant interaction was observed, the interaction effect was removed from the model and corrected using the original FDR
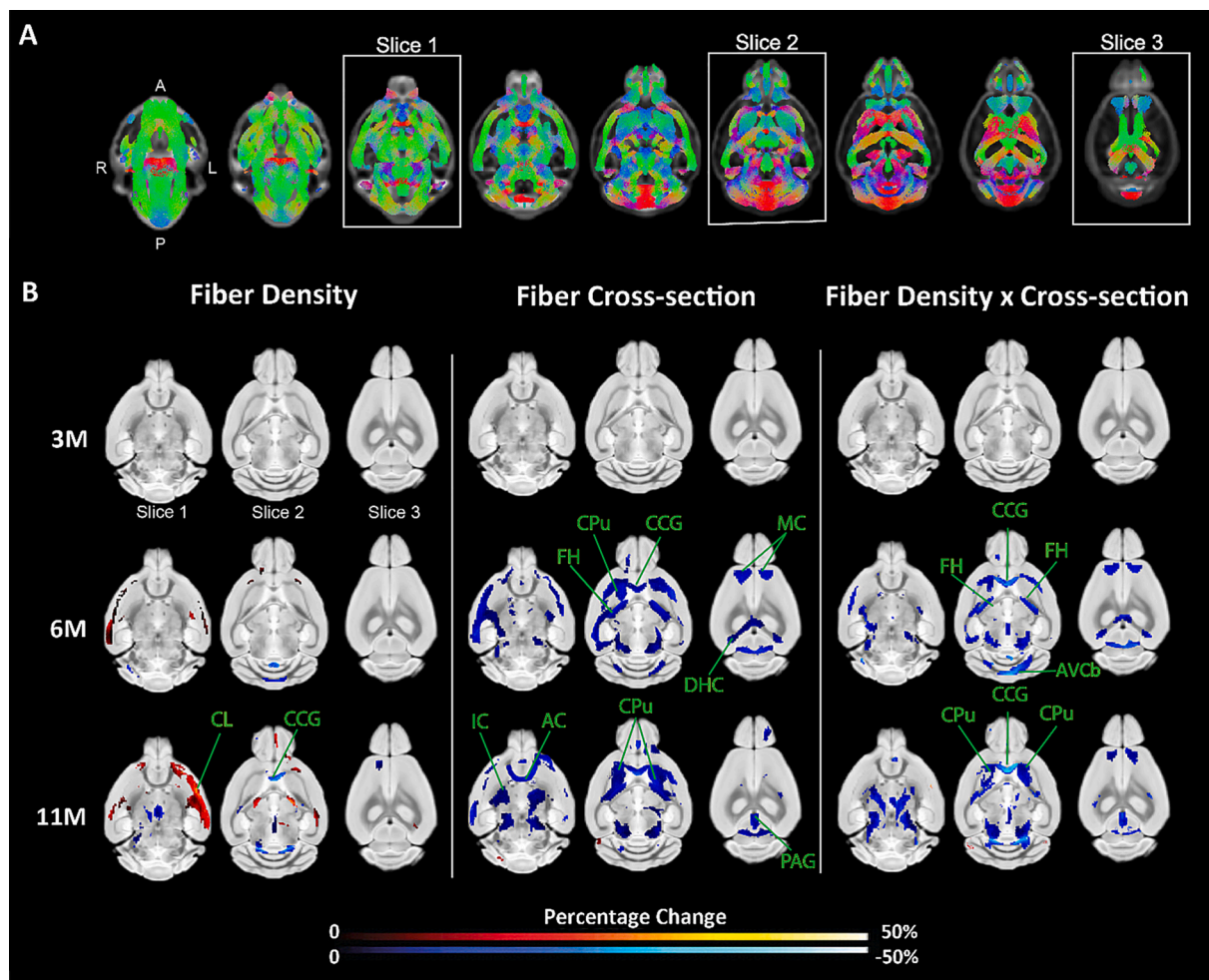
Fig. 1. Comparison of FBA metrics at different states of disease progression in the zQ175DN mouse model. (**A**) Slice-by-slice overview of tractogram overlaid on top of WMFOD map. Slices 1, 2, and 3 show the slices selected for visualization in panel B. (**B**) Streamlines showing significant (P$_{TFCE-FWE}$ < 0.05) genotype effects were overlaid on top of a T2-weighted anatomical background image at three bregma levels (Bregma −4, −2, and − 1 mm). The hot absolute effect scale indicates an increase in HET mice compared to WT mice, while cool scales indicate a significant decrease. *AC = Anterior commissure, AVCb = arbor vitae of the cerebellum, CPu = Caudate putamen, CL = Claustrum, CCG = Corpus callosum genu, DHC = Dorsal hippocampal commissure, FH = Fimbria of the hippocampus, IC = Internal capsule, MC = Motor cortex, PAG = Periaqueductal gray.*

method. NfL values were logarithmically transformed, then log(NfL) and diffusion metrics were converted to control normalized z-scores. A Pearson correlation analysis was performed between the control normalized z-scores of NfL values with control normalized z-scores of diffusion metrics in MATLAB 2021a.

LFB-stained image intensities in the corpus callosum genu were analyzed using a two-way ANOVA model for the effects of age (6 and 13 months of age) and genotype (WT and HET). No interaction effect was observed, therefore no post-hoc analysis was performed. The interaction term was removed from the model. All data are represented as mean ± standard deviation (SD) and statistical significance was set at $p < 0.05$.

3. Results

3.1. Fiber bundle morphology is altered in zQ175DN HET mice

First, we performed a whole-brain FBA in fiber bundles (Fig. 1A) to identify in an unbiased manner fiber bundle alterations at different ages in HET mice compared to WT littermates. This analysis revealed no significant differences for any of the metrics at 3 months of age (Fig. 1B). However, by 6 months of age, differences were observed in the metrics, namely FD, FC, and FDC. FD was higher in the cortical fibers and lower in fibers of the cerebellum of HET mice compared to WT littermates. On the contrary, FC was lower in HET mice compared to WT in widespread fiber bundles, including fibers in white matter structures such as the corpus callosum genu (CCG), internal capsule (IC), external capsule (EC), fimbria of the hippocampus (FH) and the arbor vitae of the cerebellum (AVCb) as well as gray matter structures such as the motor cortex (MC), periaqueductal gray (PAG), caudate putamen (CPu), and substantia nigra. Additionally, widespread FDC reductions were also observed in HET mice compared to WT mice at 6 months. These differences colocalized with the FC reductions but demonstrated higher magnitude in some brain regions, such as the corpus callosum genu and the arbor vitae of the cerebellum.

At 11 months of age (Fig. 1B), most areas showed a larger spatial extent of significant differences for all metrics. Noteworthy, we observed a significantly lower FD in the corpus callosum genu and an increase of FD in fibers of the claustrum (CL) in HET mice compared to WT littermates. FC was significantly lower in the anterior commissure (AC) at 11 months of age in HET compared to WT mice. No difference was observed in the FC of fibers in the motor cortex of HET mice at 11 months of age. The FDC also indicated a decrease in the corpus callosum genu of HET mice compared to WT littermates, driven by the FD difference that was present at 11 months of age.

3.2. zQ175DN HET mice display a global decrease in white matter diffusivity

Next, we assessed if global patterns as those observed in the FBA statistical maps could be measured in a whole brain white matter tissue compartment analysis of FBA and DTI metrics. Hereto we extracted the average FBA metrics and DTI metrics across all voxels within the white matter compartment (Fig. 2A). This revealed a pattern that was in line with the FBA statistical maps, FDC was decreased at 6 months (−4.78%, $p < 0.0001$) and 11 months of age (−3.06%, $p = 0.002$) in HET mice (Fig. 2B). This effect was mainly driven by the FC metrics, which was also significantly lower at 6 (−7.09%, $p < 0.0001$) and 11 months of age (−11.25%, $p < 0.0001$) (Supplementary Table 2), while FD showed an increase at 3 months of age in HET mice (1.47%, $p = 0.024$).

Unlike the FBA metrics that showed early anomalies, a significant decrease was observed in white matter FA only at 11 months of age (−2.57%, $p < 0.0001$) (Fig. 2C). The decrease in FA can be explained by a lower AD as indicated by a main effect of genotype ($F_{(1,73)} = 12.25$, $p = 0.005$) (Supplementary Table 1) and a trend towards significance for a higher RD at 11 months of age in HET mice (0.61%, $p = 0.062$) (Supplementary Table 2). Also, a lower MD was observed as indicated

by a main effect of genotype ($F_{(1,73)} = 5.89$, $p = 0.035$).

3.3. The genu of the corpus callosum displayed the most profound alterations in diffusion metrics

Based on the detected alterations in FBA metrics as well as white matter diffusivity, we focused on the analysis of the corpus callosum. The corpus callosum genu (anterior portion) showed the most pronounced difference between the genotypes for both the FBA-based FDC as well as DTI-based FA (Fig. 3B). Widespread FDC reductions in the corpus callosum genu of HET mice were detected at 6 months (−13.13%, $p < 0.0001$) and 11 months (−18.13%, $p < 0.0001$) (Fig. 3B). Similarly, FA was decreased in HET mice compared to WT at 6 (−4.67%, $p < 0.0001$) and 11 months of age (−6.08%, $p < 0.0001$). This decrease could be explained by a higher RD in HET mice at 6 and 11 months of age (3.43% and 4.09% respectively, $p < 0.0001$, Supplementary Table 2). Also, a main genotype effect for MD ($F_{(1,73)} = 9.60$, $p = 0.008$, Supplementary Table 1) was observed. An overview of the changes detected with the other metrics is available in Supplementary Table 2.

At 3 months of age, HET mice had a higher FDC (6.56%, $p = 0.017$), while at 6 months HET mice had a lower FDC (−6.63%, $p = 0.004$) compared to WT mice in the corpus callosum splenium (Fig. 3D). FC is initially increased at 3 months in the corpus callosum splenium (4.04%, $p = 0.033$), which is followed by a decrease at 6 months (−5.70%, $p = 0.004$, Supplementary Table 2) in HET mice compared to WT littermates. No differences in FA or any of the other metrics were observed in the splenium of HET mice.

3.4. Caudate putamen and motor cortex demonstrated progressive structural deficits

In addition to the corpus callosum, we also investigated the fiber populations in the caudate putamen and motor cortex given their implication in HD (Fig. 4). The fiber populations in the caudate putamen showed a reduction in FDC at 6 and 11 months of age in HET mice (−3.50%, $p = 0.047$ and −6.83%, $p < 0.0001$, respectively) (Fig. 4B). The FC metric shows a decrease already at 3 months (−2.71%, $p = 0.006$) in the caudate putamen of HET mice, progressively worsening with age (−5.65%, −6.15%, $p < 0.0001$ at 6 and 11 months, Supplementary Table 2). An FD increase was observed in HET mice at 3 months (0.23%, $p = 0.013$) and a trend towards significance at 6 months (0.06%, $p = 0.072$). Contrary to the clear FBA-based outcomes, FA nor any other DTI-based metric were able to detect significant genotypic effects in the caudate putamen (Supplementary Tables 1 & 2).

Fibers in the motor cortex showed a decreased FDC as indicated by a significant main effect of genotype ($F_{(1,73)} = 13.06$, $p = 0.0017$, Fig. 4C). FC was decreased at 6 months of age in HET mice (−9.38%, $p < 0.0001$, Supplementary Table 2). No difference was observed in the FD metric. Diffusion tensor metrics revealed a significantly lower FA at 11 months of age in the fiber bundles in the motor cortex of HET mice (−5.68%, $p < 0.0001$, Fig. 4C). AD metrics (−1.24%, $p = 0.002$ and −3.16%, $p < 0.0001$, respectively), and a significant decrease in RD at 11 months (−0.77%, $p = 0.023$) which also showed a trend towards significance at 6 months (−0.85%, $p = 0.052$) in HET mice compared to WT littermates. These changes can also explain the significant reductions at 6 and 11 months of age in the MD (−1.02%, $p = 0.004$ and −1.80%, $p < 0.0001$, respectively).

3.5. Plasma NfL is significantly increased in zQ175DN HET mice

A mixed model analysis revealed a significant interaction between the effects of age and genotype ($F_{(1,41)} = 81.30$, $p < 0.0001$). No significant difference was observed between genotypes at 6 months, but a significantly higher increased NfL protein level was observed in HET mice compared to WT littermates at 11 months of age (175.20%, $p < 0.0001$) (Fig. 5). Pearson correlation analysis performed between
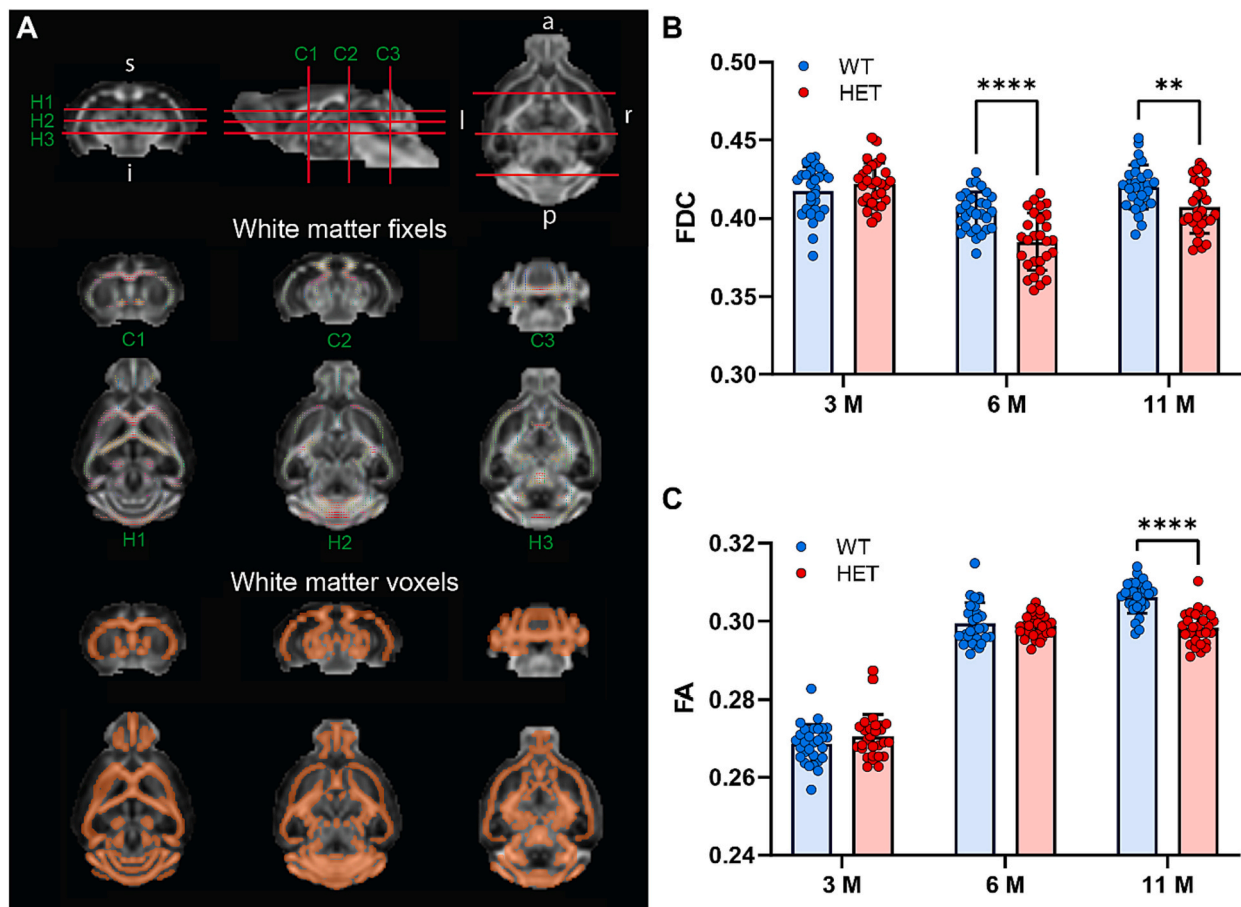
Fig. 2. Whole brain white matter analysis of voxels and fibers indicates global alterations in zQ175DN HET mice compared to WT **in the white matter tissue class**. (**A**) Three orthogonal slices indicating coronal (C1, C2, and C3) and horizontal (H1, H2, and H3) slices display white matter fixels (top rows) and white matter voxels (bottom rows). (**B**) Bar graphs represent the mean FDC value in white matter fixels of HET mice (red) compared to WT mice (blue). (**C**) Bar graphs represent the mean FA value in white matter voxels of HET mice (red) compared to WT mice (blue). Brackets indicate significant post-hoc genotype differences after FDR multiple comparisons correction. Error bars indicate *SD*. ** $p < 0.01$, **** $p < 0.0001$. s = *superior, i = inferior, l = left, r = right, a = anterior, p = posterior.* (For interpretation of the references to colour in this figure legend, the reader is referred to the web version of this article.)

control normalized log(NfL) z-scores and control normalized FDC ($r = 0$, $p = 0.983$) and FA ($r = 0.23$, $p = 0.246$) z-scores of the corpus callosum genu at 6 months reveal that there is no relationship between plasma NfL and the most prominent dMRI differences. Neither at 11 months a relationship could be observed between control normalized log(NfL) z-scores and control normalized FDC ($r = 0.04$, $p = 0.869$) and FA ($r = -0.08$, $p = 0.752$) z-scores of the corpus callosum genu.

4. Discussion

We have used traditional and advanced diffusion metrics in the zQ175DN HD mouse model at 3, 6, and 11 months of age to investigate microstructural anomalies in myelinated fiber bundles, its temporal progression, and the sensitivity of advanced FBA modeling as a potential marker for neuropathological anomalies in this HD mouse model. We demonstrated the presence of structural differences in myelinated fibers in the zQ175DN HET mouse brain at 6 months of age, with a further progression at 11 months of age. Regional anomalies in dMRI data were detected before global dMRI anomalies were found. FBA metrics could detect earlier and more prominent alterations in myelinated fiber bundles compared to the DTI metrics, supporting its use as potential marker for the investigation of HD-like phenotypic alterations in the zQ175DN mouse model.

Loss of white matter is considered a key feature of disease progression in PwHD, and global alterations in white matter features have been reported after clinical motor diagnosis, including white matter volume

decrease and global MD increases (Estevez-Fraga et al., 2023; Gregory et al., 2020; Tabrizi et al., 2011).

Our study used a measure of the whole myelinated fiber compartment to assess if such a global pattern could reveal statistically significant differences. When analyzing the myelinated fibers in the white matter compartment, using the FBA metrics, we were able to measure a statistically significant global decrease at both 6 and 11 months of age, in contrast to the DTI-based metric (FA) showing a difference only at 11 months of age.

We show that, in the zQ175DN mouse model, the most affected region is the genu of the corpus callosum, a finding in line with recent work in the Q140 HD mouse model (Pérot et al., 2022), as well as an earlier report demonstrating an anterior to posterior sensitivity of the corpus callosum in the R6/1 transgene HD model (Gatto et al., 2021). In PwHD, some studies report that the anterior part of the corpus callosum is most affected (Klöppel et al., 2008), while other studies suggest that the corpus callosum body (medial) is earliest affected (Rosas et al., 2006) and show a decrease in FA and increase in RD (Phillips et al., 2016). Taken together, these findings support the utility of diffusion-weighted imaging in the corpus callosum and suggest its potential as a biomarker of disease monitoring and HD-modifying treatments.

It is reported that changes in myelin density result in altered water diffusivity, as detected by dMRI (Casella et al., 2020; Song et al., 2002), thus an LFB staining was performed to rule out whether changes in myelin occurred in the corpus callosum genu. As shown in **Supplementary Fig. 2**, the myelin content of the corpus callosum genu did not
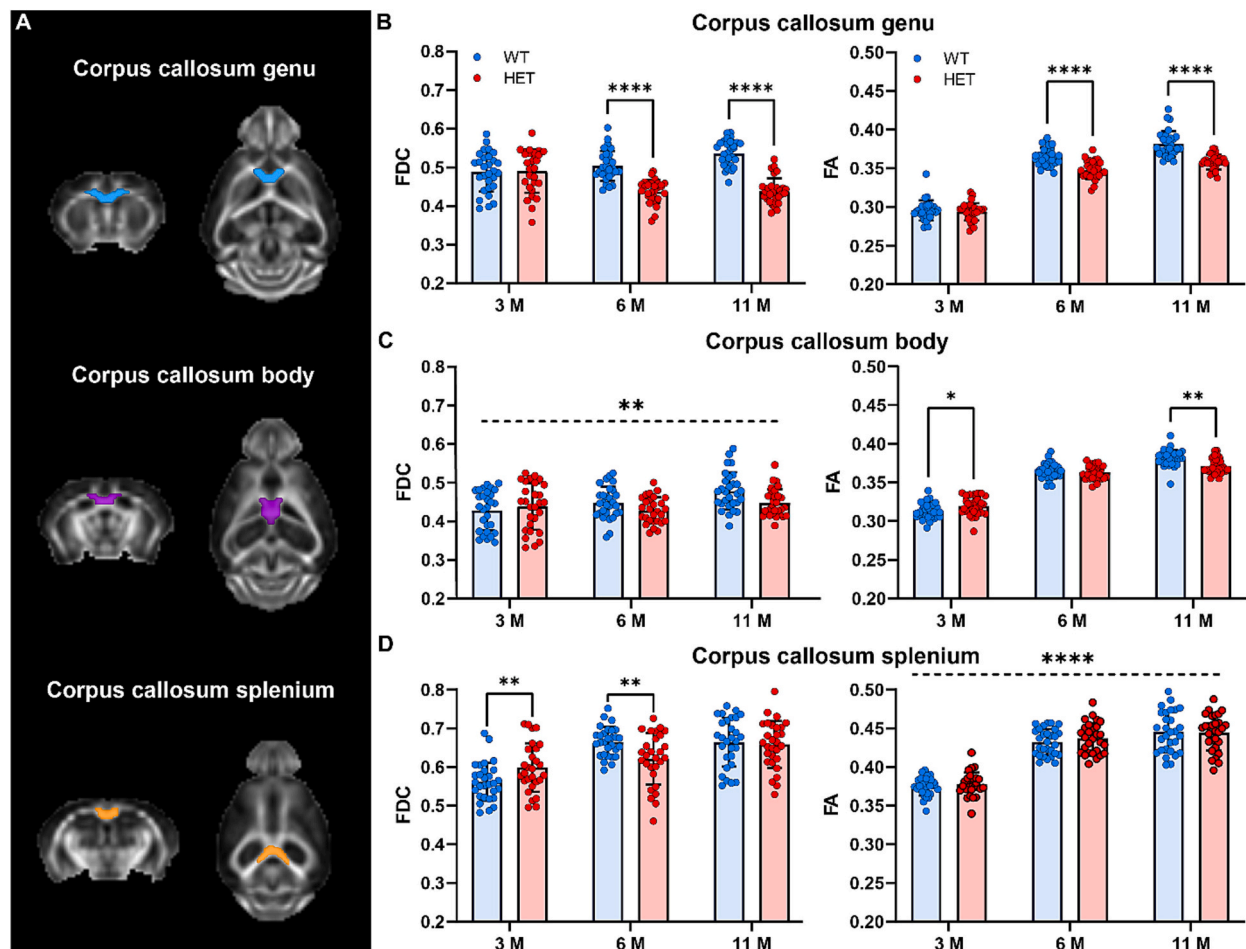
Fig. 3. **Region of interest analysis of the FDC and FA metric in the corpus callosum (genu, body, and splenium).** (**A**) Overview of regions of interest; corpus callosum genu (blue), body (purple), and splenium (orange). (**B**) Bar graphs represent the mean FDC and FA value in corpus callosum genu value for HET mice (red) compared to WT (blue) mice. (**C**) Bar graphs represent the mean FDC and FA value in the corpus callosum body for HET mice (red) compared to WT (blue) mice. (**D**) Bar graphs represent the mean FDC and FA value in corpus callosum splenium for HET mice (red) compared to WT (blue) mice. Dashed line indicates significant main age effect and brackets indicates significant post-hoc genotype effects per age after FDR multiple comparisons correction. Error bars indicate *SD*. * $p < 0.05$, ** $p < 0.01$, **** $p < 0.0001$. (For interpretation of the references to colour in this figure legend, the reader is referred to the web version of this article.)

differ between genotypes.

Another important factor contributing to the alterations in water diffusivity is the size and shape of axons which is maintained by the cytoskeleton. Neurofilament is a crucial constituent of the cytoskeleton and regulates axon caliber and mechanical support of the cytoskeleton (Yuan et al., 2017). When neurofilament loss occurs in axons, their structural integrity could become compromised (Nihei and Kowall, 1992; Vickers et al., 2016). Increased axonal tortuosity leads to a less coherent directional preference of water diffusivity and therefore to reduced FA values (Nilsson et al., 2012). This has been demonstrated in the rapidly progressing HD mouse model R6/2, where tortuosity is markedly increased in callosal fibers (Gatto et al., 2019). This interpretation was supported by the increased plasma NfL protein levels observed at 11 months of age in HET mice. Neurofilament light chains are structural elements of axons, known to be increased in cerebrospinal fluid (Constantinescu et al., 2009; Wild et al., 2015) and plasma (Byrne et al., 2017) in PwHD, and therefore proposed as prognostic biomarkers in HD (Rodrigues et al., 2021; Scahill et al., 2020). Increased levels of NfL have also been observed in rodent models of HD such as the R6/2 model, which were also correlated with disease severity (Soylu-Kucharz et al., 2017).

NfL protein levels are significantly increased at 11 months of age in zQ175DN HET mice, but not at 6 months of age, indicating that structural deficits can be detected using dMRI, prior to plasma NfL elevation

in the zQ175DN mouse model. A possible explanation is that the detection of axonal damage using a peripheral marker (plasma NfL) is slower than a more local readout of axonal integrity using dMRI.

Together with the finding that no difference was observed using LFB to quantify myelination in the corpus callosum genu, we conclude that the observed differences are mainly driven by axonal pathology itself rather than demyelination. This is contrary to many findings in other human HD studies and studies in rodent model mimicking the HD phenotype, mainly reporting white matter related anomalies which result in subsequent axonal damage (Casella et al., 2020). Further ultrastructural investigation, e.g. electron microscopy, could elucidate the precise morphological changes that occur in myelinated fiber bundles in the zQ175DN model.

The caudate putamen is considered a hallmark region in HD and consists of a complex structure containing predominantly D1 and D2 medium spiny projection neurons and traversing myelinated fiber bundles that connect the basal ganglia circuit to the cortex, thalamus, and many more structures (Fazl and Fleisher, 2018). The fixels that were modeled in our study in the caudate putamen, connect the motor cortex to the basal ganglia. These are known connections of the cortico-striatal pathway which have been demonstrated using diffusion MRI tractography and tracer studies (Allen atlas) (Pérot et al., 2022). Alterations to the cortico-striatal projections inhibit their ability to relay information and potentially lead to the motor pathology of HD in zQ175DN, which is
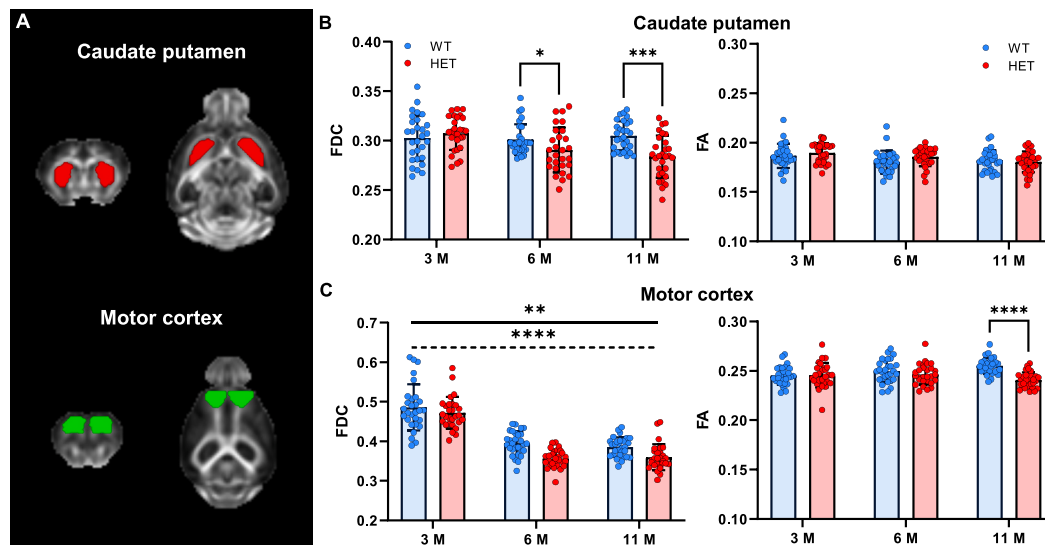
Fig. 4. Region of interest analysis of the FDC and FA metric in the caudate putamen and motor cortex. (**A**) Overview of regions of interest; caudate putamen (red) and motor cortex (green). (**B**) Bar graphs represent the mean FDC and FA value in the caudate putamen for HET (red) compared to WT (blue) mice. (**C**) Bar graphs represent the mean FDC and FA value in the motor cortex for HET (red) compared to WT (blue) mice. Dashed line indicates significant age effect, the horizontal filled line indicates a significant genotype effect (flat filled line), and brackets indicate significant post-hoc genotype differences after FDR multiple comparisons correction. Error bars indicate *SD*. * $p < 0.05$, ** $p < 0.01$, *** $p < 0.001$ **** $p < 0.0001$. (For interpretation of the references to colour in this figure legend, the reader is referred to the web version of this article.)
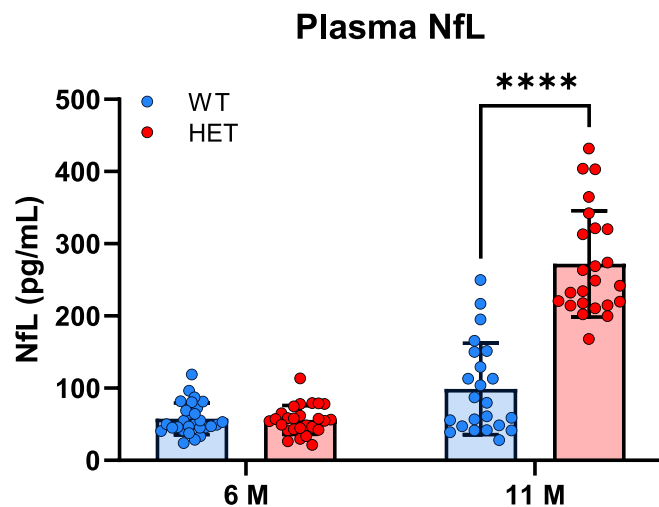
Fig. 5. Comparison of neurofilament light chain (NfL) protein in plasma of zQ175DN WT and HET mice at 6 and 11 months of age. Bar graphs represent the mean NfL value (pg/mL) for HET (red) compared to WT (blue) mice. Bracket indicates significant post-hoc genotype differences after FDR multiple comparisons correction. Error bars indicate *SD*. **** $p < 0.0001$. (For interpretation of the references to colour in this figure legend, the reader is referred to the web version of this article.)

first observed at approximately 6 months of age (Wu et al., 2022). However, progressive reductions in FC in the caudate putamen start at 3 months, suggesting it is appearing in parallel to local accumulation of mHTT aggregates and loss of phosphodiesterase 10A (Bertoglio et al., 2022a), preceding the known macrostructural changes (Heikkinen et al., 2012). The appearance of widespread changes at 6 months of age was anticipated given that most molecular, cellular, behavioral, cognitive, and brain functional changes appear at this age (Farrar et al., 2014; Heikkinen et al., 2020b; Ibrahim et al., 2023; Vasilkovska et al., 2023; Zarate et al., 2023), also reflected in the body weight loss (**Supplementary Fig. 3**) (Wu et al., 2022). Our findings also reveal a progressive pathology, which is in line with the progressive nature of HD (Bertoglio

et al., 2018; Bertoglio et al., 2022b; Häggkvist et al., 2017), leading to mHTT aggregation in intracellular and intranuclear inclusions (Bertoglio et al., 2022a, Southwell et al., 2016). The earliest progressive change was observed in the fiber-cross section metric at 3 months of age in the caudate putamen. This could therefore be explored and potentially proposed as an early biomarker of HD.

Global decreases in FDC at 6 months also precede the decrease in FA observed at 11 months of age using the more commonly used DTI, further supporting that FBA could be an earlier, more sensitive marker. Similarly, regional observations in fibers of the corpus callosum and myelinated fibers of the caudate putamen show that the FDC metric is more sensitive to detect genotypic differences compared to FA.

However, FBA requires a high angular resolution diffusion imaging (HARDI) acquisition, i.e. high b-values (2000 s/mm^2) and sufficient diffusion directions to improve the estimation of fiber density and resolve crossing fibers (Raffelt et al., 2017b), and therefore requires longer scan times. It provides improved sensitivity compared to DTI thanks to the multiple diffusion shells incorporating more information to model crossing fibers with a minimal threshold of FD. Despite the longer diffusion acquisition, the approach can easily be translated to clinical studies and a similar acquisition has already been used in clinical studies of PwHD to perform FBA (Adanyeguh et al., 2021; Oh et al., 2021; Zeun et al., 2022). Adanyeguh et al. found that fixel-based metrics (FD, FC and FDC) are reduced, which was further supported by diffusion-weighted magnetic resonance spectroscopy (DW-MRS) showing intra-axonal damage, decreased FA and increased RD in white matter tracts (Adanyeguh et al., 2021). In all studies using FBA to study HD, decreased fixel-based metrics in the cortico-striatal/spinal tracts are observed in the HD population before and after clinical motor diagnosis (Adanyeguh et al., 2021; Oh et al., 2021; Zeun et al., 2022). Our work demonstrating the ability of FBA to detect white matter abnormalities in the zQ175DN mouse model, strengthens the interest in exploring FBA-based endpoints as response biomarkers in preclinical and clinical HD studies.

However, the choice of FBA parameter is an important consideration, as we have observed that some parameters (e.g. FDC in the corpus callosum splenium) show a non-monotonic temporal change. Similarly, we previously reported a non-monotonic decrease in resting state brain functional connectivity, which is lower at 6 months of age, but not present at 10 months of age (Vasilkovska et al., 2023). Liu et al. observed

a flip in directionality of differences in cerebral blood volume in zQ175 mice from 3 to 9 months of age, possibly due to compensatory mechanisms occurring at 3 months of age (Liu et al., 2021). It is important to mention that while FBA is a sensitive method, which does not require a priori assumptions for modeling of dMRI data, this method does not offer a direct biological interpretation of underlying pathological processes, such as those driving the observed non-monotonic changes in the corpus callosum splenium. Future studies investigating therapeutic effects on FBA markers in the zQ175DN are encouraged to include sufficient timepoints to investigate such non-monotonic changes.

A limitation of this study is the use of only male mice. In rodent models, sex differences have been reported with more pronounced striatal deficits in male HD rats (Bode et al., 2008) and male Q175 HD mice (Padovan-Neto et al., 2019). Future studies including both male and female zQ175DN HET mice, in combination with the above described *post-mortem* readouts of tissue ultrastructure or localized readouts of NfL are encouraged.

5. Conclusion

By using FBA in the zQ175DN mouse model, we have shown the presence of micro- and macrostructural deficits in white matter fibers that occur in brain regions that are typically affected by mHTT-driven pathology. Progressive myelinated fiber alterations can be detected in the corpus callosum genu and caudate putamen prior to behavioral impairments using FBA metrics but not DTI metrics. The spatiotemporal progressive alterations in myelinated fiber bundles can be measured noninvasively using diffusion MRI. Altogether, further exploration of FBA-based endpoints as response biomarkers in preclinical and HD clinical studies is encouraged. The higher sensitivity of FBA to detect white matter anomalies than DTI metrics, suggests a potential benefit of adopting these advanced metrics in biomarker development in humans.

Supplementary data to this article can be found online at https://doi.org/10.1016/j.nbd.2024.106438.

CRediT authorship contribution statement

Nicholas Vidas-Guscic: Writing – review & editing, Writing – original draft, Visualization, Software, Methodology, Investigation, Formal analysis, Data curation, Conceptualization. **Joëlle van Rijswijk:** Writing – review & editing, Writing – original draft, Visualization, Software, Methodology, Investigation, Formal analysis, Conceptualization. **Johan Van Audekerke:** Validation, Software, Methodology, Formal analysis. **Ben Jeurissen:** Writing – review & editing, Software, Methodology. **Israel Nnah:** Writing – original draft, Methodology. **Haiying Tang:** Writing – review & editing, Conceptualization. **Ignacio Muñoz-Sanjuan:** Writing – review & editing, Conceptualization. **Dorian Pustina:** Writing – review & editing, Conceptualization. **Roger Cachope:** Writing – review & editing, Resources, Conceptualization. **Annemie Van der Linden:** Writing – review & editing, Supervision, Funding acquisition, Conceptualization. **Daniele Bertoglio:** Writing – review & editing, Supervision, Conceptualization. **Marleen Verhoye:** Writing – review & editing, Supervision, Project administration, Methodology, Funding acquisition, Conceptualization.

Declaration of competing interest

DP, HT, and RC are employed by CHDI Management, Inc., the company that manages the scientific activities of CHDI Foundation, Inc. CHDI Foundation, Inc., is a privately-funded nonprofit biomedical research organization exclusively dedicated to collaboratively developing therapeutics that improve the lives of those affected by Huntington's disease. No other potential conflicts of interest relevant to this article exist.

Data availability

The data presented in this paper is available on Mendeley Data, V1, doi: 10.17632/p25nzh85zp.1

References

Adanyeguh, I.M., Branzoli, F., Delorme, C., Méneret, A., Monin, M.L., Luton, M.P., Durr, A., Sabidussi, E., Mochel, F., 2021. Multiparametric characterization of white matter alterations in early stage Huntington disease. Sci. Rep. 11 (1) https://doi.org/10.1038/s41598-021-92532-1.

Andersson, J.L.R., Sotiropoulos, S.N., 2016. An integrated approach to correction for off-resonance effects and subject movement in diffusion MR imaging. NeuroImage 125, 1063–1078. https://doi.org/10.1016/j.neuroimage.2015.10.019.

Andersson, J.L.R., Skare, S., Ashburner, J., 2003. How to correct susceptibility distortions in spin-echo echo-planar images: application to diffusion tensor imaging. NeuroImage 20 (2), 870–888. https://doi.org/10.1016/S1053-8119(03)00336-7.

Atherton, J.F., Mciver, E.L., Mullen, M.R., Wokosin, D.L., Surmeier, J., Bevan, M.D., 2016. Early Dysfunction and Progressive Degeneration of the Subthalamic Nucleus in Mouse Models of Huntington's Disease. https://doi.org/10.7554/eLife.21616.001.

Basser, P.J., Mattiello, J., LeBihan, D., 1994. Estimation of the effective self-diffusion tensor from the NMR spin Echo. J. Magn. Reson. 103, 247–254.

Bates, G.P., Dorsey, R., Gusella, J.F., Hayden, M.R., Kay, C., Leavitt, B.R., Nance, M., Ross, C.A., Scahill, R.I., Wetzel, R., Wild, E.J., Tabrizi, S.J., 2015. Huntington disease. Nat. Rev. Dis. Prim. 1 (April), 1–21. https://doi.org/10.1038/nrdp.2015.5.

Beaumont, V., Zhong, S., Lin, H., Xu, W.J., Bradaia, A., Steidl, E., Gleyzes, M., Wadel, K., Buisson, B., Padovan-Neto, F.E., Chakraborty, S., Ward, K.M., Harms, J.F., Beltran, J., Kwan, M., Ghavami, A., Häggkvist, J., Tóth, M., Halldin, C., Munoz-Sanjuan, I., 2016. Phosphodiesterase 10A inhibition improves cortico-basal ganglia function in Huntington's disease models. Neuron 92 (6), 1220–1237. https://doi.org/10.1016/j.neuron.2016.10.064.

Bertoglio, D., Kosten, L., Verhaeghe, J., Thomae, D., Wyffels, L., Stroobants, S., Wityak, J., Dominguez, C., Mrzljak, L., Staelens, S., 2018. Longitudinal characterization of mGluR5 using 11C-ABP688 PET imaging in the Q175 mouse model of Huntington disease. J. Nucl. Med. 59 (11), 1722–1727. https://doi.org/10.2967/jnumed.118.210658.

Bertoglio, D., Bard, J., Hessmann, M., Liu, L., Gärtner, A., De Lombaerde, S., Huscher, B., Zajicek, F., Miranda, A., Peters, F., Herrmann, F., Schaertl, S., Vasilkovska, T., Brown, C.J., Johnson, P.D., Prime, M.E., Mills, M.R., Van der Linden, A., Mrzljak, L., Munoz-Sanjuan, I., 2022a. Development of a ligand for in vivo imaging of mutant huntingtin in Huntington's disease. Sci. Transl. Med. 14, 3682. https://www.science.org.

Bertoglio, D., Verhaeghe, J., Wyffels, L., Miranda, A., Stroobants, S., Mrzljak, L., Dominguez, C., Skinbjerg, M., Bard, J., Liu, L., Munoz-Sanjuan, I., Staelens, S., 2022b. Synaptic vesicle glycoprotein 2A is affected in the central nervous system of mice with Huntington disease and in the brain of a human with Huntington disease postmortem. J. Nucl. Med. 63 (6), 942–947. https://doi.org/10.2967/jnumed.121.262709.

Bode, F.J., Stephan, M., Suhling, H., Pabst, R., Straub, R.H., Raber, K.A., Bonin, M., Nguyen, H.P., Riess, O., Bauer, A., Sjoberg, C., Petersén, Å., von Hörsten, S., 2008. Sex differences in a transgenic rat model of Huntington's disease: decreased 17β-estradiol levels correlate with reduced numbers of DARPP32+ neurons in males. Hum. Mol. Genet. 17 (17), 2595–2609. https://doi.org/10.1093/hmg/ddn159.

Byrne, L.M., Rodrigues, F.B., Blennow, K., Durr, A., Leavitt, B.R., Roos, R.A.C., Scahill, R.I., Tabrizi, S.J., Zetterberg, H., Langbehn, D., Wild, E.J., 2017. Neurofilament light protein in blood as a potential biomarker of neurodegeneration in Huntington's

disease: a retrospective cohort analysis. Lancet Neurol. 16 (8), 601–609. https://doi.org/10.1016/S1474-4422(17)30124-2.

Byrne, L.M., Rodrigues, F.B., Johnson, E.B., Wijeratne, P.A., De Vita, E., Alexander, D.C., Palermo, G., Czech, C., Schobel, S., Scahill, R.I., Heslegrave, A., Zetterberg, H., Wild, E.J., 2018. Evaluation of mutant huntingtin and neurofilament proteins as potential markers in Huntington's disease. In Sci. Transl. Med 10. https://www.science.org.

Callahan, J.W., Wokosin, D.L., Bevan, M.D., 2022. Dysregulation of the basal ganglia indirect pathway in early symptomatic Q175 Huntington's disease mice. J. Neurosci. 42 (10), 2080–2102. https://doi.org/10.1523/JNEUROSCI.0782-21.2022.

Casella, C., Lipp, I., Rosser, A., Jones, D.K., Metzler-Baddeley, C., 2020. A Critical Review of White Matter Changes in Huntington's Disease. https://doi.org/10.1002/mds.28109.

Constantinescu, R., Romer, M., Oakes, D., Rosengren, L., Kieburtz, K., 2009. Levels of the light subunit of neurofilament triplet protein in cerebrospinal fluid in Huntington's disease. Parkinsonism Relat. Disord. 15 (3), 245–248. https://doi.org/10.1016/j.parkreldis.2008.05.012.

Covey, D.P., Dantrassy, H.M., Zlebnik, N.E., Gildish, I., Cheer, J.F., 2016. Compromised dopaminergic encoding of reward accompanying suppressed willingness to overcome high effort costs is a prominent prodromal characteristic of the Q175 mouse model of huntington's disease. J. Neurosci. 36 (18), 4993–5002. https://doi.org/10.1523/JNEUROSCI.0135-16.2016.

Cudalbu, C., McLin, V.A., Lei, H., Duarte, J.M.N., Rougemont, A.L., Oldani, G., Terraz, S., Toso, C., Gruetter, R., 2013. The C57BL/6J mouse exhibits sporadic congenital portosystemic shunts. PLoS One 8 (7). https://doi.org/10.1371/journal.pone.0069782.

Deng, Y., Wang, H., Joni, M., Sekhri, R., Reiner, A., 2021. Progression of basal ganglia pathology in heterozygous Q175 knock-in Huntington's disease mice. J. Comp. Neurol. 529 (7), 1327–1371. https://doi.org/10.1002/cne.25023.

Dhollander, T., Mito, R., Raffelt, D., Connelly, A., 2019. Improved white matter response function estimation for 3-tissue constrained spherical deconvolution. In: Conference: 27th International Society of Magnetic Resonance in Medicine. https://www.researchgate.net/publication/331165168.

Dhollander, T., Clemente, A., Singh, M., Boonstra, F., Civier, O., Duque, J.D., Egorova, N., Enticott, P., Fuelscher, I., Gajamange, S., Genc, S., Gottlieb, E., Hyde, C., Imms, P., Kelly, C., Kirkovski, M., Kolbe, S., Liang, X., Malhotra, A., Caeyenberghs, K., 2021a. Fixel-based analysis of diffusion MRI: Methods, applications, challenges and opportunities. In: NeuroImage, vol. 241. Academic Press Inc. https://doi.org/10.1016/j.neuroimage.2021.118417

Dhollander, T., Tabbara, R., Rosnarho-Tornstrand, J., Tournier, J.-D., Raffelt, D., Connelly, A., 2021b. A Multi-tissue log-domain intensity and inhomogeneity normalisation for quantitative apparent fibre density. In: In Proc. ISMRM, p. 2472.

D'hollander, T., Raffelt, D., Connelly, A., 2016. Unsupervised 3-tissue response function estimation from single-shell or multi-shell diffusion MR data without a co-registered T1 image Review of Fixel-Based Analysis (FBA) of diffusion MRI (dMRI) View project. https://www.researchgate.net/publication/307863133.

Estevez-Fraga, C., Flower, M.D., Tabrizi, S.J., 2020. Therapeutic strategies for Huntington's disease. Curr. Opin. Neurol. 33 (4), 508–518. NLM (Medline). https://doi.org/10.1097/WCO.0000000000000835.

Estevez-Fraga, C., Scahill, R., Rees, G., Tabrizi, S.J., Gregory, S., 2021. Diffusion imaging in Huntington's disease: comprehensive review. J. Neurol. Neurosurg. Psychiatry 92 (1), 62–69. https://doi.org/10.1136/jnnp-2020-324377.

Estevez-Fraga, C., Elmalem, M.S., Papoutsi, M., Durr, A., Rees, E.M., Hobbs, N.Z., Roos, R.A.C., Landwehrmeyer, B., Leavitt, B.R., Langbehn, D.R., Scahill, R.I., Rees, G., Tabrizi, S.J., Gregory, S., 2023. Progressive alterations in white matter microstructure across the timecourse of Huntington's disease. Brain Behav. 1–13 https://doi.org/10.1002/brb3.2940.

Farrar, A.M., Murphy, C.A., Paterson, N.E., Oakeshott, S., He, D., Alosio, W., McConnell, K., Menalled, L.B., Ramboz, S., Park, L.C., Howland, D., Brunner, D., 2014. Cognitive deficits in transgenic and knock-in HTT mice parallel those in Huntington's disease. J. Huntington's Dis. 3 (2), 145–158. https://doi.org/10.3233/JHD-130061.

Farshim, P.P., Bates, G.P., 2018. Mouse models of Huntington's disease. In: Methods in Molecular Biology, vol. 1780. Humana Press Inc., pp. 97–120. https://doi.org/10.1007/978-1-4939-7825-0_6

Fazl, A., Fleisher, J., 2018. Anatomy, physiology, and clinical syndromes of the basal ganglia: A brief review. Semin. Pediatr. Neurol. 25, 2–9. https://doi.org/10.1016/j.spen.2017.12.005.

Ferguson, M.W., Kennedy, C.J., Palpagama, T.H., Waldvogel, H.J., Faull, R.L.M., Kwakowsky, A., 2022. Current and possible future therapeutic options for Huntington's disease. J. Central Nervous Syst. Dis. 14 https://doi.org/10.1177/11795735221092517, 117957352210925.

Gatto, R.G., Ye, A.Q., Colon-Perez, L., Mareci, T.H., Lysakowski, A., Price, S.D., Brady, S.T., Karaman, M., Morfini, G., Magin, R.L., 2019. Detection of axonal degeneration in a mouse model of Huntington's disease: comparison between diffusion tensor imaging and anomalous diffusion metrics. MAGMA 32 (4), 461–471. https://doi.org/10.1007/s10334-019-00742-6.

Gatto, R.G., Weissmann, C., Amin, M., Angeles-López, Q.D., García-Lara, L., Castellanos, L.C.S., Deyoung, D., Segovia, J., Mareci, T.H., Uchitel, O.D., Magin, R.L., 2021. Evaluation of early microstructural changes in the R6/1 mouse model of Huntington's disease by ultra-high field diffusion MR imaging. Neurobiol. Aging 102, 32–49. https://doi.org/10.1016/j.neurobiolaging.2021.02.006.

Goodliffe, J.W., Song, H., Rubakovic, A., Chang, W., Medalla, M., Weaver, C.M., Luebke, J.I., 2019. Differential changes to D1 and D2 medium spiny neurons in the 12-month-old Q175+/− mouse model of Huntington's disease. PLoS One 13 (8). https://doi.org/10.1371/journal.pone.0200626.

Gregory, S., Johnson, E., Byrne, L.M., Rodrigues, F.B., Henderson, A., Moss, J., Thomas, D., Zhang, H., De Vita, E., Tabrizi, S.J., Rees, G., Scahill, R.I., Wild, E.J., 2020. Characterizing white matter in Huntington's disease. Move. Disorders Clin. Pract. 7 (1), 52–60. https://doi.org/10.1002/mdc3.12866.

Häggkvist, J., Tóth, M., Tari, L., Varnäs, K., Svedberg, M., Forsberg, A., Nag, S., Dominguez, C., Munoz-Sanjuan, I., Bard, J., Wityak, J., Varrone, A., Halldin, C., Mrzljak, L., 2017. Longitudinal small-animal PET imaging of the zQ175 mouse model of Huntington disease shows in vivo changes of molecular targets in the striatum and cerebral cortex. J. Nucl. Med. 58 (4), 617–622. https://doi.org/10.2967/jnumed.116.180497.

Heikkinen, T., Lehtimäki, K., Vartiainen, N., Puoliväli, J., Hendricks, S.J., Glaser, J.R., Bradaia, A., Wadel, K., Touller, C., Kontkanen, O., Yrjänheikki, J.M., Buisson, B., Howland, D., Beaumont, V., Munoz-Sanjuan, I., Park, L.C., 2012. Characterization of neurophysiological and behavioral changes, MRI brain Volumetry and 1H MRS in zQ175 Knock-in mouse model of Huntington's disease. PLoS One 7 (12). https://doi.org/10.1371/journal.pone.0050717.

Heikkinen, T., Bragge, T., Bhattarai, N., Parkkari, T., Puoliväli, Jukka, Kontkanen, O., Sweeney, P., Park, L.C., Munoz-Sanjuan, I., 2020a. Rapid and robust patterns of spontaneous locomotor deficits in mouse models of Huntington's disease. PLoS One 15 (12 December), 1–21. https://doi.org/10.1371/journal.pone.0243052.

Heikkinen, T., Bragge, T., Bhattarai, N., Parkkari, T., Puoliväli, Jukka, Kontkanen, O., Sweeney, P., Park, L.C., Munoz-Sanjuan, I., 2020b. Rapid and robust patterns of spontaneous locomotor deficits in mouse models of Huntington's disease. PLoS One 15 (12 December), 1–21. https://doi.org/10.1371/journal.pone.0243052.

Herrmann, F., Hessmann, M., Schaertl, S., Berg-Rosseburg, K., Brown, C.J., Bursow, G., Chiki, A., Ebneth, A., Gehrmann, M., Hoeschen, N., Hotze, M., Jahn, S., Johnson, P. D., Khetarpal, V., Kiselyov, A., Kottig, K., Ladewig, S., Lashuel, H., Letschert, S., Bard, J.A., 2021. Pharmacological characterization of mutant huntingtin aggregate-directed PET imaging tracer candidates. Sci. Rep. 11 (1) https://doi.org/10.1038/s41598-021-97334-z.

Ibrahim, K.S., El Mestikawy, S., Abd-Elrahman, K.S., Ferguson, S.S.G., 2023. VGLUT3 deletion rescues motor deficits and neuronal loss in the zQ175 mouse model of Huntington's disease. J. Neurosci. Off. J. Soc. Neurosci. April. https://doi.org/10.1523/JNEUROSCI.0014-23.2023.

Jeurissen, B., Leemans, A., Sijbers, J., 2014a. Automated correction of improperly rotated diffusion gradient orientations in diffusion weighted MRI. Med. Image Anal. 18 (7), 953–962. https://doi.org/10.1016/j.media.2014.05.012.

Jeurissen, B., Tournier, J.D., Dhollander, T., Connelly, A., Sijbers, J., 2014b. Multi-tissue constrained spherical deconvolution for improved analysis of multi-shell diffusion MRI data. NeuroImage 103, 411–426. https://doi.org/10.1016/j.neuroimage.2014.07.061.

Johnson, E.B., Byrne, L.M., Gregory, S., Rodrigues, F.B., Blennow, K., Durr, A., Leavitt, B. R., Roos, R.A., Zetterberg, H., Tabrizi, S.J., Scahill, R.I., Wild, E.J., 2018. Neurofilament light protein in blood predicts regional atrophy in Huntington disease. Neurology 90 (8), e717–e723. https://doi.org/10.1212/WNL.0000000000005005.

Kellner, E., Dhital, B., Kiselev, V.G., Reisert, M., 2016. Gibbs-ringing artifact removal based on local subvoxel-shifts. Magn. Reson. Med. 76 (5), 1574–1581. https://doi.org/10.1002/mrm.26054.

Klöppel, S., Draganski, B., Golding, C., Chu, C., Nagy, Z., Cook, P.A., Hicks, S.L., Kennard, C., Alexander, D.C., Parker, G.J.M., Tabrizi, S.J., Frackowiak, R.S.J., 2008. White matter connections reflect changes in voluntary-guided saccades in pre-symptomatic Huntington's disease. Brain 131 (1), 196–204. https://doi.org/10.1093/brain/awm275.

Langfelder, P., Cantle, J.P., Chatzopoulou, D., Wang, N., Gao, F., Al-Ramahi, I., Lu, X.H., Ramos, E.M., El-Zein, K., Zhao, Y., Deverasetty, S., Tebbe, A., Schaab, C., Lavery, D. J., Howland, D., Kwak, S., Botas, J., Aaronson, J.S., Rosinski, J., Yang, X.W., 2016. Integrated genomics and proteomics define huntingtin CAG length-dependent networks in mice. Nat. Neurosci. 19 (4), 623–633. https://doi.org/10.1038/nn.4256.

Lee, H., Fenster, R.J., Pineda, S.S., Gibbs, W.S., Mohammadi, S., Davila-Velderrain, J., Garcia, F.J., Therrien, M., Novis, H.S., Gao, F., Wilkinson, H., Vogt, T., Kellis, M., LaVoie, M.J., Heiman, M., 2020. Cell type-specific transcriptomics reveals that mutant huntingtin leads to mitochondrial RNA release and neuronal innate immune activation. Neuron 107 (5), 891–908.e8. https://doi.org/10.1016/j.neuron.2020.06.021.

Liu, H., Zhang, C., Xu, J., Jin, J., Cheng, L., Miao, X., Wu, Q., Wei, Z., Liu, P., Lu, H., Van Zijl, P.C.M., Ross, C.A., Hua, J., Duan, W., 2021. Huntingtin silencing delays onset and slows progression of Huntington's disease: A biomarker study. Brain 144 (10), 3101–3113. https://doi.org/10.1093/brain/awab190.

MacDonald, M.E., Ambrose, Christine M., Duyao, Mabel P., Myers, Richard H., Lin, Carol, Srinidhi, Lakshmi, Barnes, Glenn, Taylor, Sherry A., James, Marianne, Groat, Nicolet, MacFarlane, Heather, Jenkins, Barbara, Anderson, Mary Anne, Wexler, Nancy S., Gusella, James F., 1993. A novel gene containing a trinucleotide repeat that is expanded and unstable on Huntington's disease chromosomes. Cell 72, 971–983.

Menalled, L.B., Kudwa, A.E., Miller, S., Fitzpatrick, J., Watson-Johnson, J., Keating, N., Ruiz, M., Mushlin, R., Alosio, W., McConnell, K., Connor, D., Murphy, C., Oakeshott, S., Kwan, M., Beltran, J., Ghavami, A., Brunner, D., Park, L.C., Ramboz, S., Howland, D., 2012. Comprehensive behavioral and molecular characterization of a new Knock-in mouse model of Huntington's disease: ZQ175. PLoS One 7 (12). https://doi.org/10.1371/journal.pone.0049838.

Nihei, K., Kowall, N.W., 1992. Neurofilament and neural cell adhesion molecule immunocytochemistry of Huntington's disease striatum. Ann. Neurol. 31 (1), 59–63. https://doi.org/10.1002/ana.410310111.

Nilsson, M., Lätt, J., Ståhlberg, F., van Westen, D., Hagslätt, H., 2012. The importance of axonal undulation in diffusion MR measurements: A Monte Carlo simulation study. NMR Biomed. 25 (5), 795–805. https://doi.org/10.1002/nbm.1795.

Oakeshott, S., Port, R., Cummins-Sutphen, J., Berger, J., Watson-Johnson, J., Ramboz, S., Paterson, N., Kwak, S., Howland, D., Brunner, D., 2012. A mixed fixed ratio/progressive ratio procedure reveals an apathy phenotype in the BAC HD and the z_Q175 KI mouse models of Huntington's disease. PLoS Curr. 4, e4f972cffe82c0 https://doi.org/10.1371/4f972cffe82c0.

Oh, S.L., Chen, C.M., Wu, Y.R., Valdes Hernandez, M., Tsai, C.C., Cheng, J.S., Chen, Y.L., Wu, Y.M., Lin, Y.C., Wang, J.J., 2021. Fixel-based analysis effectively identifies white matter tract degeneration in Huntington's disease. Front. Neurosci. 15 https://doi.org/10.3389/fnins.2021.711651.

Padovan-Neto, F.E., Jurkowski, L., Murray, C., Stutzmann, G.E., Kwan, M., Ghavami, A., Beaumont, V., Park, L.C., West, A.R., 2019. Age- and sex-related changes in cortical and striatal nitric oxide synthase in the Q175 mouse model of Huntington's disease. Nitric Oxide 83, 40–50. https://doi.org/10.1016/j.niox.2018.12.002.

Pérot, J.-B., Célestine, M., Palombo, M., Dhenain, M., Humbert, S., Brouillet, E., Flament, J., 2022. Longitudinal multimodal MRI characterization of a knock-in mouse model of Huntington's disease reveals early grey and white matter alterations. Hum. Mol. Genet. https://doi.org/10.1093/hmg/ddac036/6526656.

Phillips, O.R., Joshi, S.H., Squitieri, F., Sanchez-Castaneda, C., Narr, K., Shattuck, D.W., Caltagirone, C., Sabatini, U., di Paola, M., 2016. Major superficial white matter abnormalities in Huntington's disease. Front. Neurosci. 10 (MAY) https://doi.org/10.3389/fnins.2016.00197.

Piiponniemi, T.O., Parkkari, T., Heikkinen, T., Puoliväli, J., Park, L.C., Cachope, R., Kopanitsa, M.V., 2018. Impaired performance of the Q175 mouse model of huntington's disease in the touch screen paired associates learning task. Front. Behav. Neurosci. 12 https://doi.org/10.3389/fnbeh.2018.00226.

Raffelt, D., Tournier, J.D., Rose, S., Ridgway, G.R., Henderson, R., Crozier, S., Salvado, O., Connelly, A., 2012. Apparent fibre density: A novel measure for the analysis of diffusion-weighted magnetic resonance images. NeuroImage 59 (4), 3976–3994. https://doi.org/10.1016/j.neuroimage.2011.10.045.

Raffelt, D.A., Smith, R.E., Ridgway, G.R., Tournier, J.D., Vaughan, D.N., Rose, S., Henderson, R., Connelly, A., 2015. Connectivity-based fixel enhancement: whole-brain statistical analysis of diffusion MRI measures in the presence of crossing fibres. NeuroImage 117, 40–55. https://doi.org/10.1016/j.neuroimage.2015.05.039.

Raffelt, D., Dhollander, T., Tournier, J.D., Tabbara, R., Smith, R.E., Pierre, E., Connelly, A., 2017a. Bias field correction and intensity normalisation for quantitative analysis of apparent fibre density. In: Proc. ISMRM.

Raffelt, D.A., Tournier, J.D., Smith, R.E., Vaughan, D.N., Jackson, G., Ridgway, G.R., Connelly, A., 2017b. Investigating white matter fibre density and morphology using fixel-based analysis. NeuroImage 144, 58–73. https://doi.org/10.1016/j.neuroimage.2016.09.029.

Reijmer, Y.D., Leemans, A., Heringa, S.M., Wielaard, I., Jeurissen, B., Koek, H.L., Biessels, G.J., 2012. Improved sensitivity to cerebral white matter abnormalities in Alzheimer's disease with spherical deconvolution based tractography. PLoS One 7 (8). https://doi.org/10.1371/journal.pone.0044074.

Rodrigues, F.B., Byrne, L.M., Tortelli, R., Johnson, E.B., Wijeratne, P.A., Arridge, M., De Vita, E., Ghazaleh, N., Furby, H., Alexander, D.C., Tabrizi, S.J., Schobel, S., Scahill, R.I., Heslegrave, A., Zetterberg, H., Wild, E.J., 2021. Europe PMC Funders Group Europe PMC Funders Author Manuscripts Europe PMC Funders Author Manuscripts Mutant huntingtin and neurofilament light have distinct longitudinal dynamics in Huntington ' s disease, vol. 12 (574). https://doi.org/10.1126/scitranslmed.abc2888.Mutant.

Rosas, H.D., Tuch, D.S., Hevelone, N.D., Zaleta, A.K., Vangel, M., Hersch, S.M., Salat, D. H., 2006. Diffusion tensor imaging in presymptomatic and early Huntington's disease: selective white matter pathology and its relationship to clinical measures. Mov. Disord. 21 (9), 1317–1325. https://doi.org/10.1002/mds.20979.

Scahill, R.I., Zeun, P., Osborne-Crowley, K., Johnson, E.B., Gregory, S., Parker, C., Lowe, J., Nair, A., O'Callaghan, C., Langley, C., Papoutsi, M., McColgan, P., Estevez-Fraga, C., Fayer, K., Wellington, H., Rodrigues, F.B., Byrne, L.M., Heselgrave, A., Hyare, H., Tabrizi, S.J., 2020. Biological and clinical characteristics of gene carriers far from predicted onset in the Huntington's disease young adult study (HD-YAS): a cross-sectional analysis. Lancet Neurol. 19 (6), 502–512. https://doi.org/10.1016/S1474-4422(20)30143-5.

Schneider, C.A., Rasband, W.S., Eliceiri, K.W., 2012. NIH image to ImageJ: 25 years of image analysis. Nat. Methods 9 (7), 671–675. https://doi.org/10.1038/nmeth.2089.

Skare, S., Bammer, R., 2009. Jacobian Weighting of Distortion Corrected EPI Data.

Smarr, B., Cutler, T., Loh, D.H., Kudo, T., Kuljis, D., Kriegsfeld, L., Ghiani, C.A., Colwell, C.S., 2019. Circadian dysfunction in the Q175 model of Huntington's disease: network analysis. J. Neurosci. Res. 97 (12), 1606–1623. https://doi.org/10.1002/jnr.24505.

Smith, S.M., Jenkinson, M., Woolrich, M.W., Beckmann, C.F., Behrens, T.E.J., Johansen-Berg, H., Bannister, P.R., de Luca, M., Drobnjak, I., Flitney, D.E., Niazy, R.K., Saunders, J., Vickers, J., Zhang, Y., de Stefano, N., Brady, J.M., Matthews, P.M., 2004. Advances in functional and structural MR image analysis and implementation as FSL. NeuroImage 23 (Suppl. 1). https://doi.org/10.1016/j.neuroimage.2004.07.051.

Smith, R.E., Tournier, J.D., Calamante, F., Connelly, A., 2013. SIFT: spherical-deconvolution informed filtering of tractograms. NeuroImage 67, 298–312. https://doi.org/10.1016/j.neuroimage.2012.11.049.

Smith, G.A., Rocha, E.M., McLean, J.R., Hayes, M.A., Izen, S.C., Isacson, O., Hallett, P.J., 2014. Progressive axonal transport and synaptic protein changes correlate with

behavioral and neuropathological abnormalities in the heterozygous Q175 KI mouse model of Huntington's disease. Hum. Mol. Genet. 23 (17), 4510–4527. https://doi.org/10.1093/hmg/ddu166.

Snowden, J.S., 2017. The neuropsychology of Huntington's disease. Arch. Clin. Neuropsychol. 32 (7), 876–887. Oxford University Press. https://doi.org/10.1093/arclin/acx086.

Song, S.K., Sun, S.W., Ramsbottom, M.J., Chang, C., Russell, J., Cross, A.H., 2002. Dysmyelination revealed through MRI as increased radial (but unchanged axial) diffusion of water. NeuroImage 17 (3), 1429–1436. https://doi.org/10.1006/nimg.2002.1267.

Southwell, A.L., Smith-Dijak, A., Kay, C., Sepers, M., Villanueva, E.B., Parsons, M.P., Xie, Y., Anderson, L., Felczak, B., Waltl, S., Ko, S., Cheung, D., Cengio, L.D., Slama, R., Petoukhov, E., Raymond, L.A., Hayden, M.R., 2016. An enhanced Q175 knock-in mouse model of Huntington disease with higher mutant huntingtin levels and accelerated disease phenotypes. Hum. Mol. Genet. 25 (17), 3654–3675. https://doi.org/10.1093/hmg/ddw212.

Soylu-Kucharz, R., Sandelius, Å., Sjögren, M., Blennow, K., Wild, E.J., Zetterberg, H., Björkqvist, M., 2017. Neurofilament light protein in CSF and blood is associated with neurodegeneration and disease severity in Huntington's disease. Sci. Rep. 7 (1), 4–11. https://doi.org/10.1038/s41598-017-14179-1.

Tabrizi, S.J., Scahill, R.I., Durr, A., Roos, R.A.C., Leavitt, B.R., Jones, R., Bernhard Landwehrmeyer, G., Fox, N.C., Johnson, H., Hicks, S., Kennard, C., Craufurd, D., Frost, C., Langbehn, D.R., Reilmann, R., Stout, J.C., 2011. Biological and clinical changes in premanifest and early stage Huntington's disease in the TRACK-HD study: the 12-month longitudinal analysis. Lancet Neurol. 10 https://doi.org/10.1016/S1474-4422(10)70276-3.

Tournier, J.D., Calamante, F., Gadian, D.G., Connelly, A., 2004a. Direct estimation of the fiber orientation density function from diffusion-weighted MRI data using spherical deconvolution. NeuroImage 23 (3), 1176–1185. https://doi.org/10.1016/j.neuroimage.2004.07.037.

Tournier, J.D., Calamante, F., Connelly, A., 2007. Robust determination of the fibre orientation distribution in diffusion MRI: non-negativity constrained super-resolved spherical deconvolution. NeuroImage 35 (4), 1459–1472. https://doi.org/10.1016/j.neuroimage.2007.02.016.

Tustison, N.J., Avants, B.B., Cook, P.A., Zheng, Y., Egan, A., Yushkevich, P.A., Gee, J.C., 2010. N4ITK: improved N3 bias correction. IEEE Trans. Med. Imaging 29 (6), 1310–1320. https://doi.org/10.1109/TMI.2010.2046908.

Vasilkovska, T., Adhikari, M.H., Van Audekerke, J., Salajeghe, S., Pustina, D., Cachope, R., Tang, H., Liu, L., Muñoz-Sanjuán, I., Van der Linden, A., Verhoye, M., 2023. Resting-state fMRI reveals longitudinal alterations in brain network connectivity in the zQ175DN mouse model of Huntington's disease. Neurobiol. Dis. 181 (March) https://doi.org/10.1016/j.nbd.2023.106095.

Veraart, J., Sijbers, J., Sunaert, S., Leemans, A., Jeurissen, B., 2013. Weighted linear least squares estimation of diffusion MRI parameters: strengths, limitations, and pitfalls. NeuroImage 81, 335–346. https://doi.org/10.1016/j.neuroimage.2013.05.028.

Veraart, J., Fieremans, E., Novikov, D.S., 2016a. Diffusion MRI noise mapping using random matrix theory. Magn. Reson. Med. 76 (5), 1582–1593. https://doi.org/10.1002/mrm.26059.

Veraart, J., Novikov, D.S., Christiaens, D., Ades-aron, B., Sijbers, J., Fieremans, E., 2016b. Denoising of diffusion MRI using random matrix theory. NeuroImage 142, 394–406. https://doi.org/10.1016/j.neuroimage.2016.08.016.

Vickers, J.C., Kirkcaldie, M.T., Phipps, A., King, A.E., 2016. Alterations in neurofilaments and the transformation of the cytoskeleton in axons may provide insight into the aberrant neuronal changes of Alzheimer's disease. Brain Res. Bull. 126, 324–333. https://doi.org/10.1016/j.brainresbull.2016.07.012.

Vonsattel, J.-P., Myers, R.H., Stevens, T.J., Ferrante, R.J., Bird, E.D., Richardson, E.P., 1985. Neuropathological classification of Huntinqton's disease, 44 (6). https://academic.oup.com/jnen/article/44/6/559/2613653.

Wild, E.J., Henley, S.M.D., Hobbs, N.Z., Frost, C., MacManus, D.G., Barker, R.A., Fox, N. C., Tabrizi, S.J., 2010. Rate and acceleration of whole-brain atrophy in premanifest and early Huntington's disease. Mov. Disord. 25 (7), 888–895. https://doi.org/10.1002/mds.22969.

Wild, E.J., Boggio, R., Langbehn, D., Robertson, N., Haider, S., Miller, J.R.C., Zetterberg, H., Leavitt, B.R., Kuhn, R., Tabrizi, S.J., Macdonald, D., Weiss, A., 2015. Quantification of mutant huntingtin protein in cerebrospinal fluid from Huntington's disease patients. J. Clin. Invest. 125 (5), 1979–1986. https://doi.org/10.1172/JCI80743.

Wu, J., Möhle, L., Brüning, T., Eiriz, I., Rafehi, M., Stefan, K., Stefan, S.M., Pahnke, J., 2022. A novel Huntington's disease assessment platform to support future drug discovery and development. Int. J. Mol. Sci. 23 (23) https://doi.org/10.3390/ijms232314763.

Yuan, A., Rao, M.V., Veeranna, Nixon, R.A., 2017. Neurofilaments and neurofilament proteins in health and disease. Cold Spring Harb. Perspect. Biol. 9 (4) https://doi.org/10.1101/cshperspect.a018309.

Zarate, N., Gundry, K., Yu, D., Casby, J., Eberly, L.E., Öz, G., Gomez-Pastor, R., 2023. Neurochemical correlates of synapse density in a Huntington's disease mouse model. J. Neurochem. 164 (2), 226–241. https://doi.org/10.1111/jnc.15714.

Zeun, P., McColgan, P., Dhollander, T., Gregory, S., Johnson, E.B., Papoutsi, M., Nair, A., Scahill, R.I., Rees, G., Tabrizi, S.J., 2022. Timing of selective basal ganglia white matter loss in premanifest Huntington's disease. NeuroImage: Clin. 33 https://doi.org/10.1016/j.nicl.2021.102927.